Instability of a moving liquid sheet in the presence of acoustic forcing

Aditya S. Mulmule,[1] Mahesh S. Tirumkudulu,[1] and K. Ramamurthi[2]
[1]*Department of Chemical Engineering, Indian Institute of Technology-Bombay, Mumbai 400076, India*
[2]*Indian Institute of Technology-Madras, Chennai 600036, India*

(Received 13 October 2009; accepted 1 December 2009; published online 5 February 2010)

The excitation of thin planar liquid sheets formed by impinging two collinear water jets to acoustic waves was studied at varying frequencies and sound pressure levels (SPLs). Experiments were conducted over a range of liquid velocities that encompassed the stable and flapping regimes of the sheet. For a given frequency, there was a threshold value of SPL below which the sheet was unaffected. The threshold SPL increased with frequency. Further, the sheet was observed to respond to a set of specific frequencies lying in the range of 100–300 Hz, the frequency set varying with the Weber number of the liquid sheet. The magnitude of the response for a fixed pressure level, characterized by the reduction in the extent of the sheet, was larger at lower frequencies. The droplet sizes formed by the disintegration of the sheet reduced with an increase in the measured response and the drop-shedding frequency was near the imposed frequency. Model equations for inviscid flow and accounting for the varying pressure field across the moving liquid sheet of constant thickness was solved to determine the linear stability of the system. Numerical solution shows that the most unstable wavelengths in the presence of the forcing to be smaller than in the absence, which is in line with observations. Both the dilatational and sinuous modes are coupled at the lowest order and become significant for the range of acoustic forcing studied. The model calculation suggests that the parametric resonance involving the dilatational mode may be responsible for the observed instability although the model was unable to predict the observed variation of threshold SPL with frequency.
 [doi:10.1063/1.3290745]

I. INTRODUCTION

When two laminar liquid jets of equal diameter and velocity impinge head-on, the equal and opposite forces of each jet acting at the point of impact cancel each other, thereby creating a region of high pressure that spreads the liquid radially outward.[1–5] The liquid sheet, so formed, expands at the point of impact in the plane perpendicular to the direction of the two jets until it breaks up into droplets. The spread and the dynamics of such sheets are characterized by the Weber number, $\mathrm{We}=\rho_l V^2 d_o/\sigma$, that measures the competition between the inertial force driving the liquid outward and the restraining force of surface tension at the periphery of the sheet. Here, ρ_l and σ are the density and surface tension of the liquid, respectively, while V and d_o are the jet velocity and diameter, respectively. Huang[4] measured the sheet radius for varying We and identified two distinct modes of breakup of the liquid sheets comprising wavy and nonwavy processes. For $100<\mathrm{We}<500$, the liquid sheet was stable with a near-perfect circular edge. In this range of low We, the liquid collects into a thick rim at the sheet edge which subsequently disintegrates into beads and detaches from the sheet at regular intervals to form droplets. The surface of the sheet is smooth and free from oscillations. A force balance at the circular edge along with a mass balance relating the jet diameter (d_o) to the sheet diameter (D) gives[2,3]

$$\frac{D}{d_o}=\frac{\mathrm{We}}{4}, \tag{1}$$

which shows that the sheet diameter increases with We. When We is increased to values $500<\mathrm{We}<800$, the disturbances at the point of impingement create capillary waves on the sheet that propagate radially outward. These waves, also known as cardioid waves,[6] converge at the periphery resulting in cusp-shaped edge of the liquid sheet instead of the circular edge observed at lower values of We. For yet higher values of We ($800<\mathrm{We}<2000$), a steady transition occurs from the stable sheet regime to the flapping regime.

When the We exceeds 800, the liquid sheet becomes distinctly unstable and oscillates/flaps like a membrane. Here the sheet diameter reduces with increasing We.[4,7]

Squire[1] showed that when a thin liquid film moves relative to a gas, the interfaces become unstable due to the Kelvin–Helmholtz (KH) instability, and the deformation of the two interfaces gives rise to two different wave modes, viz., antisymmetric and symmetric waves (Fig. 1). A simple scaling analysis shows that the growth rates of the two modes are related as[8,9] $\gamma_D \sim (h/\lambda)\gamma_S$, where γ_S and γ_D are the growth rates for the dilatational (symmetric) and sinuous (antisymmetric) waves, h is the sheet thickness, and λ is the wavelength. As the ratio h/λ is less than unity in most cases, the sinuous waves tend to dominate the breakup process.

Based on the maximum unstable growth rate calculated by Squire,[1] Villermaux and Clanet[7] showed the sheet diameter to vary as

$$\frac{D}{d_o}\sim\left(\frac{\rho_l}{\rho_a}\right)^{2/3}\mathrm{We}^{-1/3}, \tag{2}$$

where ρ_a is the density of the surrounding gas. Further, the droplet size, d, decreases with We for the stable regime,

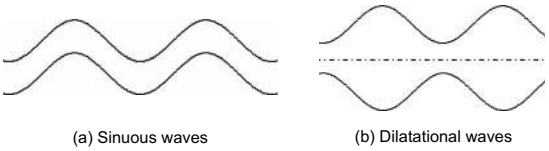

FIG. 1. Wave modes in a thin liquid sheet.

$$\frac{d}{d_o} \sim \mathrm{We}^{-1/3}, \tag{3}$$

while the undulatory motion of the sheet in the flapping regime causes the liquid sheet to disintegrate at a substantially smaller scale via indentations of the rim from which small droplets detach. The drop size also decays much faster with increasing jet velocity in the flapping regime of the sheet than in the stable regime and is given by

$$\frac{d}{d_o} \sim \left(\frac{\rho_a}{\rho_l}\right)^{-2/3} \mathrm{We}^{-1}. \tag{4}$$

While most of the previous work has focused on the dynamics of liquids sheets, only a few have investigated the influence of external disturbances on the sheet. Rhys[10] studied the influence of acoustics on the stability of the sheet. Sound waves emanating from a speaker impinged on a flat liquid sheet produced from a rectangular orifice. The influence of sound frequency, sound intensity, and liquid velocity on the sheet dynamics was determined. It was observed that at a fixed decibel level, the sheet response was significant at low frequencies. Also, at a fixed frequency, the amplitude of sheet undulation/flapping increased with the sound intensity. Sivadas *et al.*[11] introduced acoustic disturbances in the coaxial flow of air over the top and bottom surfaces of a planar liquid sheet. The breakup length was seen to be a good measure of the stability of the liquid sheet. A characteristic breakup frequency was identified as the frequency at which large amplitude waves grow to break up the liquid sheet. The influence of the acoustic disturbance was greater for $\mathrm{We}_s \equiv \rho_l V^2 h/\sigma < 9$, for which the momentum transfer from the air to the liquid sheet is smaller.

Bremond *et al.*[12] recently studied the atomization of circular liquid sheets where a solid vertical cylinder on which a jet impacts is oscillated at a controlled frequency and amplitude. The vibrating cylinder results in an undulated sheet where both the frequency and amplitude of the sheet can be set independently. Experiments were performed in both the stable and flapping regimes and the sheet diameter reduced under this forcing. They observed fluid droplets ejected from preferential sites on the sheet rim although they do not report a shedding frequency for the droplets. For a given We, they distinguished a stable and an unstable forcing regime based on a critical forcing frequency. The latter was derived by first equating the real part of the sinuous mode[1] to the forcing frequency while simultaneously setting the growth rate (imaginary part) to zero. While the latter gives the wavenumber at neutral instability, the two relations together give a critical frequency below which the sheet is unstable,

$$\frac{\omega_c}{d_o} V = \mathrm{We}\left(\frac{\rho_a}{\rho_l}\right)\left(1 - \frac{4}{\mathrm{We}}\right). \tag{5}$$

Note that the above relation has been modified to account for the impingement of two jets compared to a single jet in their case. They further predict the reduction in the sheet radius in the presence of external forcing by determining the growth rate of transverse sheet undulations due to the vertical acceleration caused by the difference in the liquid and sinuous wave velocity. This "wavy corridor" mechanism, which results from the Rayleigh–Taylor (RT) instability of the thin sheet, predicts a decrease in the sheet radius with increasing forcing frequency for a given forcing amplitude and jet speed.

The study reported here is motivated by the need to understand the atomization of liquid sheets in the presence of external disturbances. The formation of sprays using impinging liquid jets is preferred in a number of different applications considering the flexibility to vary the degree of atomization and mixing. The unsteadiness of sprays formed from impinging jets and the interaction with external disturbances often causes combustion instability problems in high power density combustors. The present study addresses the influence of the external acoustic waves on the dynamics of liquid sheets produced from impinging liquid jets. A series of experiments were conducted with water sheets formed by the head-on impingement of laminar jets. The influence of acoustic waves of different frequencies on the disintegration and the size of droplets formed by the disintegration for the stable and flapping regimes of the sheet were determined. A stability analysis of the liquid sheet that included the effects of the liquid motion and external pressure is carried out to interpret the experimental results. The analysis shows that for the range of system parameters applicable for our experimental conditions, the dilatational and sinuous modes couple, and unlike the Squire case, results in dilatational growth rates equal in magnitude to that of the sinuous mode. The response at the select frequencies is also attributed to the dilatational mode as the corresponding growth rates vary significantly with respect to the external forcing frequency.

II. EXPERIMENTAL SETUP

Figure 2 shows the experimental setup. The nozzles, made of borosilicate glass with an exit diameter close to 2 mm and length of 20 mm, were used to form laminar jets. The nozzles were mounted on three-dimensional (3D) traverses and could be rotated using rotating stages. The diameter of the jet was determined accurately from photographs obtained with a high-speed camera and was determined to be 2.175 mm. The jets were observed to remain laminar up to a distance of 3 mm from the nozzle at the highest value of We used in the experiments. The two nozzles were placed 4 mm apart opposite to each other along a common center line.

A continuous supply of water was obtained from overhead tanks situated at a height of around 16 m with respect to the experimental setup. The flow rate in each nozzle was measured with the help of rotameters of capacity 0.1–1 and

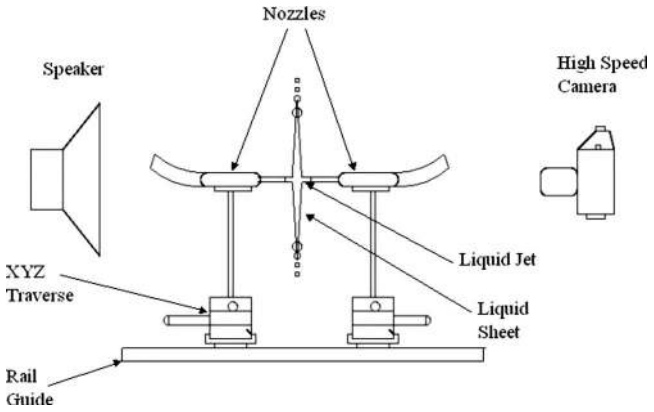

FIG. 2. Schematic of the apparatus used.

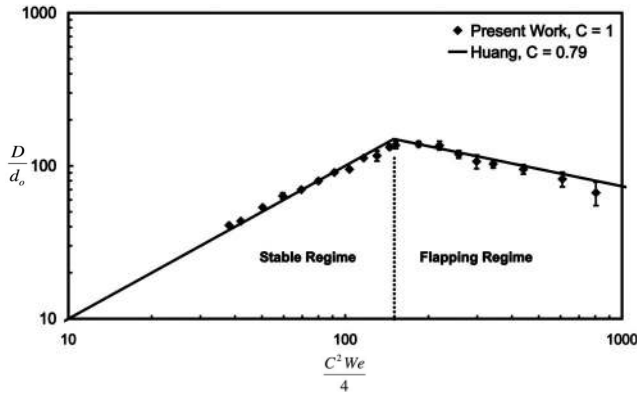

FIG. 3. Comparison of present work with that of Huang (Ref. 4). Here C is the coefficient of contraction.

0.4–4 l/min, which had an uncertainty of ±0.2% of full scale. Care was taken to remove the air bubbles trapped inside the pipeline. The liquid sheet was illuminated with 1000 W halogen lamps and the images of the sheet were captured on a Redlake Motion Pro® high-speed camera (Fig. 2). Acoustic waves were generated using a high decibel performance speaker [Ahuja VS 200®, a 200 W RMS speaker with a maximum sound pressure level (SPL) of 125 dB]. The speaker was placed normal to the liquid sheet at a distance of 60 cm (Fig. 2). The speaker was capable of delivering sound of frequencies ranging from 65 to 18 000 Hz.

Since the experiments were focused on studying the changes in the diameter of the sheet and the subsequent changes in the pattern of droplet ejection, the speaker and the camera were placed on the opposite sides of the liquid sheet. Care was taken to ensure that the center of the speaker was located along the axis of the nozzles so that the intensity of the acoustic wave was uniform over the entire sheet.

An extensive image analysis was performed to study the liquid sheet atomization phenomenon in the absence as well as in the presence of acoustic field. The sheet diameter was determined using about 1000 images recorded at a frame rate of 500 frames/s. These images were averaged by overlapping all the images over each other using MATLAB's® image analysis modules. The diameter of the sheet in the averaged image was then used in the analysis. Further, there was an over all error of 5% in the measurement of the sheet diameter from a single image while converting pixel dimensions on the image to distance units. The study of the effect of acoustic forcing on the droplet shedding frequency and the drop size distribution was also performed using images recorded on the high-speed camera.

A. Effect of acoustic field on the diameter of the liquid sheet

The accuracy of the results was checked by comparing the results obtained in the absence of acoustics with those from earlier investigations. The dimensionless diameter of the sheet (D/d_o), determined in the absence of the acoustic field, is plotted against C^2 We/4, where C is the coefficient of contraction of the jet (Fig. 3). The solid line represents Huang's results corrected by C while the points represent the present experimental measurements. The value of C^2 We/4 is used since in the experiments of Huang, the liquid jet was detached from the nozzle and the effective Weber number was based on the diameter of the nozzle. The diameter of the jet was the product of the coefficient of contraction and the orifice diameter. In the present set of experiments, the jet is attached to the nozzle. The plots show that the measurements agree with his results for both the steady and flapping breakup regimes thereby confirming the accuracy of the measurements.

The response of the sheet to the acoustic pressure disturbance was quantified by the reduction in the diameter of the sheet. The various stages of sheet breakup are shown in Fig. 4 where the images are separated by a short time interval. On switching on the acoustics, surface ripples are observed all over the sheet and they appear to travel downstream toward the edge. Within a short time after switching on the acoustics, radial streaks originate about 4–5 cm away from the edge of sheet and expand toward the edge of the sheet. This can be seen close to the circumference of the sheet in Figs. 4(b) and 4(c) and is highlighted with arrows in Fig. 5 to show that the distance between the streaks is approximately constant. As soon as the ends of the streaks reach the circum-

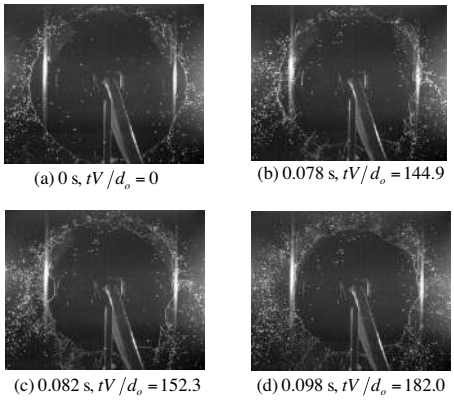

FIG. 4. The images present the breakup of the sheet at We=492 in the presence of acoustics for 150 Hz ($\omega d_o/V$=0.51) and 111 dB (Pd_o/σ =0.21), where P is the root mean square pressure. Image (a) represents the first image where a ripple was observed on the sheet surface after the acoustics was turned on.

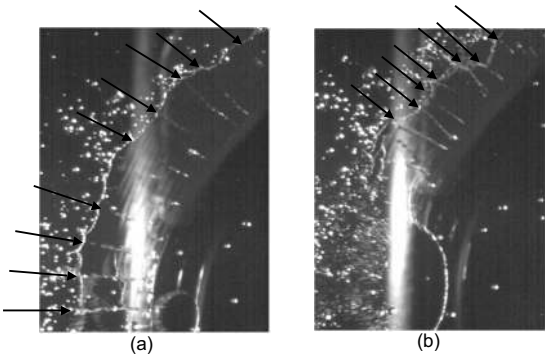

FIG. 5. A close-up of the radial streaks observed in the second quadrant of the liquid sheet in (a) Fig. 4(b) and (b) Fig. 4(c). The arrows highlight the position of the streaks.

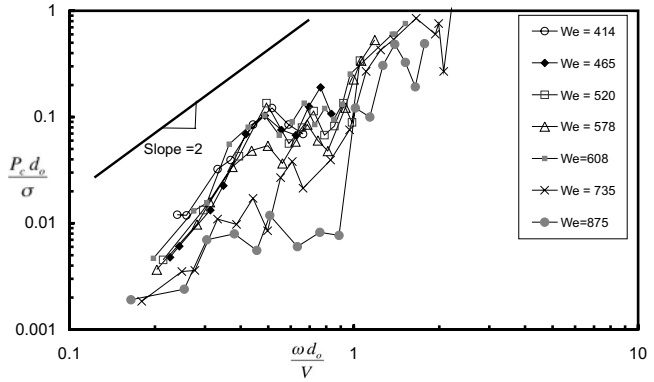

FIG. 7. The root mean square threshold SPL (P_c) is plotted against frequency for various Weber numbers in the stable sheet regime.

ference, the sheet diameter starts to reduce while tiny jets of water are ejected from the circumference of the sheet. The streaks then almost disappear as in Fig. 4(d). In some cases, falling droplets may induce a perforation [as seen in Fig. 4(b) at the nine o'clock position] in the sheet followed by an immediate reduction in the sheet diameter. The formation of a hole is a clear indication of the pinching of the sheet. The sheet finally reduces in diameter to a stable size under acoustic forcing [Fig. 4(d)] where the radial streaks vanish. The drops either simply detach from the rim or are ejected as a fine spray at discrete locations along the rim.

Figures 6(a) and 6(b) show two steady-state images of liquid sheet at We=875 taken in absence and in the presence of acoustic waves of frequency 160 Hz at 100 dB. The average diameter of the sheet reduced from 302 to 206 mm under the influence of acoustic forcing with a significant increase in the number of droplets. A closer inspection of the two images also seemed to indicate that the size of the droplets had decreased.

A similar response is seen at We=492 when the liquid sheet is influenced by acoustic waves of 110 Hz at 100 dB [Fig. 6(c) and 6(d)]. Here, the lighting arrangement was changed so as to highlight the ripples on the sheet surface induced by the acoustics. The wavy surface is seen as bright

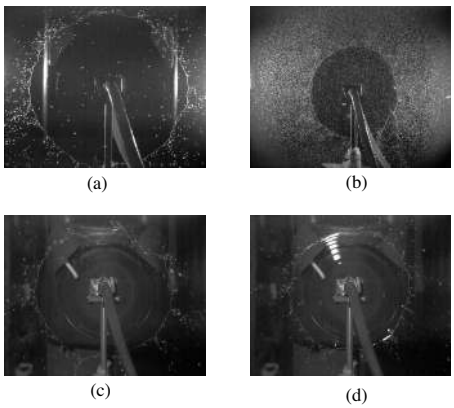

FIG. 6. Photographs of the liquid sheet at We=875, 160 Hz ($\omega d_o/V=0.32$) (a) in the absence and (b) in the presence of acoustics (100 dB, $Pd_o/\sigma=0.06$) and at We=492, 110 Hz ($\omega d_o/V=0.37$) (c) in the absence and (d) in the presence of acoustics (100 dB, $Pd_o/\sigma=0.06$). The lighting in the latter case is changed to reveal the surface undulations.

bands along the azimuthal direction in the upper half of the sheet [Fig. 6(d)]. The SPL acting on the sheet can be calculated from the definition of sound intensity, $\mathrm{dB}=20\log_{10}[P/(2\times10^{-5})]$, where P is the root mean square SPL in pascal. For varying We, Fig. 7 plots the threshold SPL, in dimensionless form ($P_c d_o/\sigma$), for decibel levels ranging from 70 dB (0.002) to 125 dB (1.0) against the forcing frequency. Here, P_c denotes the value of pressure only above which the sheet responds (i.e., size is reduced) to the external forcing. In these experiments, the frequency was fixed and the decibel level at which the sheet responded was recorded. The experiments were conducted for varying We with measurements made at increments of 20 Hz. The value of P_c for all We increases with frequency. As We increases at a fixed frequency, the value of P_c reduces. These observations can be physically interpreted by noting that the sheet is displaced perpendicular to its interface by the oscillating external pressure field. Balancing the external pressure with the inertia of the film gives the magnitude of the acceleration as, $\delta\omega^2 \sim P/\rho_l h$, where δ is the characteristic displacement of the sheet. If we assume that a given liquid sheet will break up only when the magnitude of the acceleration is above a critical value, then the critical pressure should vary as the square of the frequency. The solid line in Fig. 7 is drawn with a slope of 2 suggesting that the observations follow this trend. A more careful examination of the trend however indicates that it is nonmonotonic between 100 and 300 Hz with the sheet responding more readily to some select frequencies in that range. For example, the nondimensional SPL for We=578 increases from 0.035 to 0.1 and then decreases to 0.04 at $\omega d_o/V=0.8$ before rising again at higher frequencies. This seems to suggest a possibility that the film resonates with the forcing frequency at select frequencies.

In order to conduct a more extensive study of the influence of the acoustics on the sheet disintegration, we henceforth report experiments where the decibel level was fixed at 100 dB ($Pd_o/\sigma=0.06$) and the response of the sheet was recorded for varying frequency. The experiments were repeated several times to ensure the reproducibility of the results.

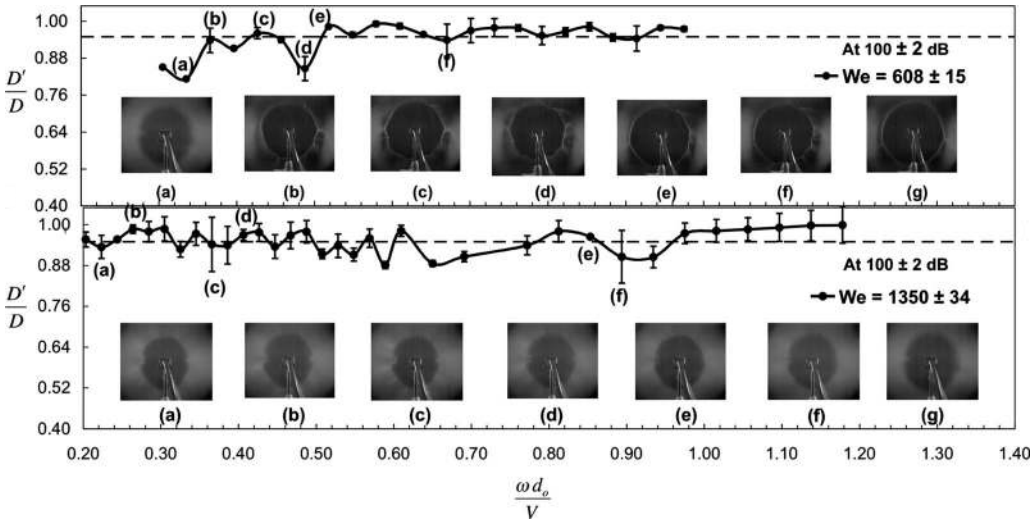

FIG. 8. The normalized sheet diameter for We=608 and 1350 subjected to varying frequencies at 100 dB. The images show the response of the sheet. Image (g) in both cases shows the sheet in the absence of forcing. The error bars account for the spatial and temporal variation in the size of the sheet.

B. Response of the sheet to acoustics

The change in the diameter of the sheet is a good quantitative measure of the response of the sheet to acoustic forcing. A detailed image analysis was performed to quantify it. Experiments were performed at two different We in the stable regime (We$<$800), viz., We=492 and 608 and two in the transition/flapping regime (We$>$800), namely, We=875 and 1350.

C. Stable sheet regime (We<800)

The top plot in Fig. 8 presents the response of the sheet to various dimensionless frequencies ($\omega d_o/V$) for We=608. The response is indicated in terms of the ratio of modified diameter (D') under the influence of acoustics to the original diameter (D) of the sheet in the absence of any acoustic forcing. Since the overall error in the sheet diameter measurement is about 5%, a horizontal line passing through 0.95 is drawn to indicate that only those frequencies with $D'/D<0.95$ are considered as a response to acoustics. It is seen that the sheet responds to only select frequencies. For example, while significant response can be observed at dimensionless frequencies of 0.33 [(a) 110 Hz] and 0.49 [(d) 160 Hz], almost no change was observed at other frequencies. The figure also includes the images of the sheet at frequencies that correspond to those indicated by (a)–(f). Image (g) corresponds to the sheet formed in absence of acoustic forcing. One of the noticeable aspects about these responses is that the sheet is maximally influenced at the lower select frequencies suggesting that the sheet resonates to these forcing frequencies. Further, the measured wavelength of the ripples on the sheet was approximately 0.011–0.014 m. When the frequency was increased beyond 320 Hz and up to 1500 Hz at 100 dB, the sheet showed no response at all. Similar set of experiments performed for We=492 (not shown in the figure) resulted in a weak response at $\omega d_o/V=0.37$ (110 Hz) and showed no response at higher frequencies. This is in line with the previous observation that the threshold SPL for breaking up the sheet increases with frequency.

D. Flapping sheet regime (We>800)

Experiments were conducted in the transition/flapping regime for We=875 and 1350. For We=875, the sheet responded to all dimensionless frequencies less than 0.91 (360 Hz) and showed no response for dimensionless frequencies above 1.12 (440 Hz). This trend is different from that observed at We=608, where response was observed only at selected frequencies. A similar observation was recorded by Rhys[10] who noted significant response at low frequencies (in his experiments, the response of the sheet to 776 Hz at 130 dB was more than at 1140 Hz at the same decibel level) for thin liquid sheets of $We_s=1100$. A near-perfect circular sheet was observed at We=875 with dimensionless frequencies of 0.27 (110 Hz) and 0.41 (160 Hz).

The response at We=1350 was different from that at We=875 in that the response was much weaker (Fig. 8). Some reduction in sheet size was observed at frequencies [0.65 (320 Hz) and 0.93 (460 Hz)] higher than those for lower We. When the frequency was increased in steps of 50 Hz from 500 to 1000 Hz, the sheet did not show any significant response.

E. Uniformity of sound intensity over liquid sheet and standing waves

Recall that a significant response was observed at 110, 160, and 220 Hz at We=608. Figure 9 presents the measured sound intensity levels at four different locations of the sheet for an average intensity of 100 dB for six different frequencies. The four measurements were made in the four quadrants of the sheet at a radial distance of 10–12 cm from the point of impingement. A comparison of the intensity distribution for 150 Hz [Fig. 9(c)] and 160 Hz [Fig. 9(d)] shows

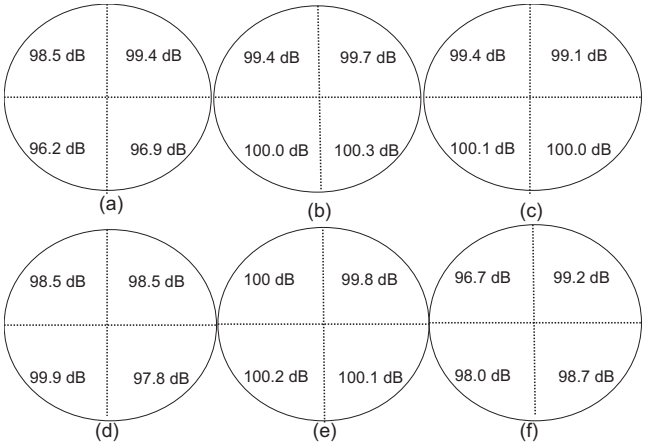

FIG. 9. Measured sound intensity levels at four locations along the sheet for 100 dB at (a) 110 Hz, (b) 130 Hz, (c) 150 Hz, (d) 160 Hz, (e) 170 Hz, and (f) 220 Hz.

that the intensity levels in the four quadrants to be slightly higher in case of 150 Hz although the response for We=608 was pronounced at 160 Hz and significantly lower at 150 Hz. The same is also true for 220 Hz where sheet breakup is observed but the reading in the four quadrants is somewhat lower than 100 dB. These observations suggest that it is not the variation of sound intensity at the sheet surface that results in pronounced response at select frequencies.

Further, we checked if the resonance could be caused by standing waves formed from the interaction of the reflected waves from the sheet with the incident excitation. As mentioned in the experimental section, the distance between the liquid sheet and the speaker is 60 cm. Since the speed of sound is about 330 m/s, the characteristic frequency of the standing wave is the quarter wave mode with a frequency of $330/(4\times0.6)=137.5$ Hz. Note that this will be the lowest frequency at which one would expect resonance with higher ones being integer multiples of 137.5 Hz. Clearly, this is not observed in our case since the resonant frequencies occur more closely.

F. Droplet shedding frequencies

Drops ejected from the periphery of the sheet were counted in a small region of interest (ROI) selected very close to the sheet's periphery in each of the captured images. This ensured that only those drops that were shed from that particular section were accounted in the analysis. Figure 10 shows two images of a section of the sheet, the first being a single raw image with the ROI next to the sheet rim and a second where the ROI in the same image has been processed by first thresholding the image so as to clearly contrast the drop against the background, using despeckle option to remove noise, and then smoothen to get whole drops. Using this procedure we were able to determine the number and size distribution of the drops in the ROI of each frame.

The drop-shedding frequency (Ω) was determined for We=608, 875, and 1350 with sound level fixed at 100 dB. The number of drops in the ROI was plotted against the

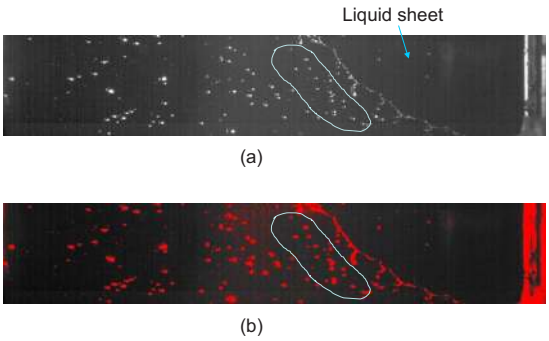

FIG. 10. (Color online) (a) An original image with ROI and (b) a processed image for determining the number and size distribution of drops. Only the ROI is processed where the threshold was set between 55 and 255 followed by despeckling and smoothening.

frame number and then the shedding frequency was evaluated using the fast Fourier transform (FFT) technique. The sound level was fixed at 100 dB in all cases. Figure 11 presents the intensity versus the frequency spectrum (Ω) in the absence and presence of acoustic forcing.

The FFT plot for We=608 (Fig. 11) shows that there are two shedding frequencies, one corresponding to the natural frequency ($\Omega d_o/V=0.1,33$ Hz) corresponding to the case of no forcing and the other close to the forcing frequency ($\Omega d_o/V=0.33,110$ Hz). The latter is indicated by the arrow in the plot. For We=875, in the absence of acoustics, there is a distinctive peak at 0.05 (20 Hz) corresponding to the natural shedding frequency. In the presence of acoustics ($\omega d_o/V=0.56,220$ Hz), a shedding frequency very close to the applied acoustic frequency is observed.

In the flapping regime, corresponding to We=1350, a weak response was observed at 440 Hz which corresponds to $\omega d_o/V=0.89$. While there is a peak close to this value, there are large peaks at several other lower frequencies. It should be noted, however, that the measurement is prone to error by the fact that We=1350 lies in the flapping regime where the

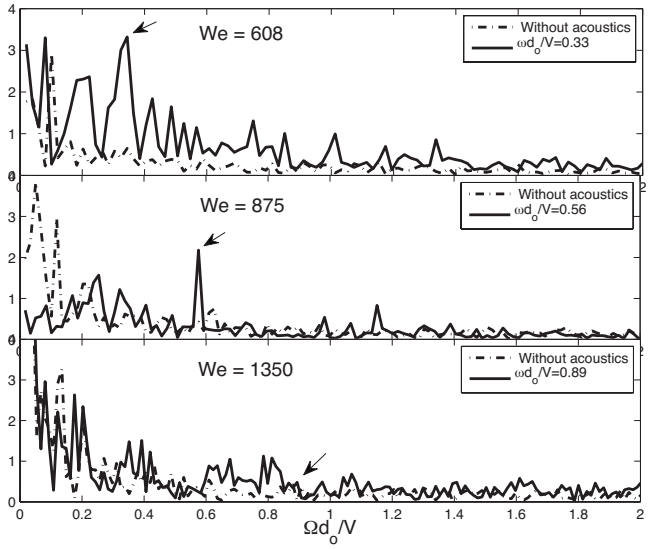

FIG. 11. Intensity vs droplet shedding frequency (Ω) in the absence and presence of acoustics for We=608, 875, and 1350. The arrows indicate the forcing frequency.

TABLE I. Mean droplet size ($\langle d\rangle/d_o$) with and without acoustics at 100 dB and varying frequency.

We	No acoustics	Maximum response	Minimum response
608	1.02	0.67	0.99
875	0.54	0.42	0.49
1350	0.37	0.32	0.34

sheet disintegration is violent and with large number of small drops being dispersed everywhere. The number of stray droplets coming into the camera frame increased significantly during this experiment which might have resulted in frequency peaks other than the forcing frequency.

G. Droplet size distribution

As in case of the shedding frequency, only the drops very close to the sheet were considered for measurements. This ensured that the droplets remained in the plane of the sheet (since the distances were calibrated in the plane of the sheet). The drop size distribution was determined for We =608, 875, and 1350 for various frequencies and decibel levels. The results for the mean dimensionless drop sizes ($\langle d\rangle/d_o$) are summarized in Table I. As We increases, the mean drop size decreases in both the stable and flapping regime and the measured sizes agree with those reported by Villermaux and Clanet.[7] The introduction of the acoustic field causes a further reduction in droplet sizes by about 35% when the sheet maximally responds to the acoustic field. In case of minimum response when the sheet diameter remains unchanged in the presence of acoustics, there is a small change in the average size confirming the fact that the acoustic waves do not significantly affect the sheet at those frequencies.

Figure 12 plots the probabililty distribution function for various forcing conditions against the dimensionless drop size. Interestingly, all the data points collapse even though the flow conditions are very different. This is in line with earlier studies which show that the distribution is universal in shape with a long exponential tail at large drop sizes. Villermaux *et al.*[13] showed that the drop size distribution,

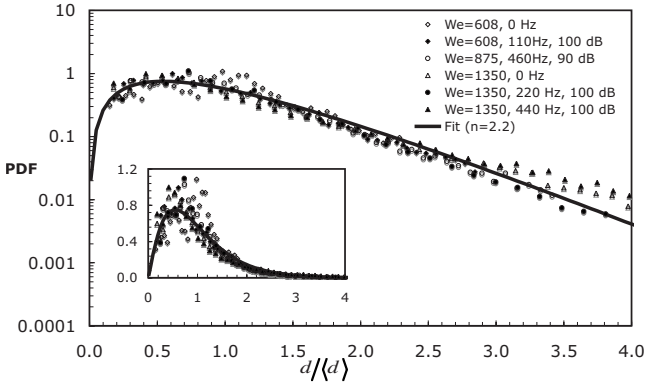

FIG. 12. PDF for drop size in the presence and absence of acoustics for varying flow and forcing conditions. The solid line is a curve fit using the gamma probability distribution (6).

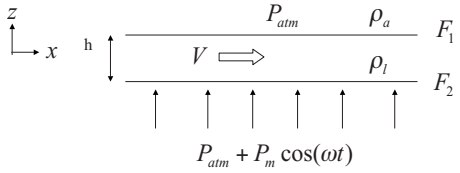

FIG. 13. Acoustic pressure acting on one side of the sheet exposed to the speaker.

irrespective of the atomization process, can be modeled by focusing on the ligament breakup process during atomization. The predicted drop size distribution follows a gamma distribution,

$$p(X) = \frac{n^n}{\Gamma(n)} X^{n-1} e^{-nX}, \quad \text{where } X = \frac{d}{\langle d\rangle}. \tag{6}$$

The experimental probability density function (PDF) obtained by Bremond *et al.*[12] for liquid sheets forced by oscillating jet impactor follows the above distribution with n lying between 4 and 5. In our case, the best fit value for n is about 2.2 indicating that the decay at large sizes is somewhat slow. This is because we are imaging a region close to the sheet rim. Large drops on dissociating from the rim/sheet edge and captured in our ROI undergo further breakup after emerging out of the ROI. Also two neighboring drops at distances less than our camera resolution (0.2 mm) will be imaged as a single large drop. Consequently, we get a small fraction of large drops ($d/\langle d\rangle > 2.5$) with PDF<0.04. Further, the smallest drop that we can image is about 0.2 mm ($d/\langle d\rangle \sim 0.2$), which corresponds to the size of 1 pixel.

III. MODEL EQUATIONS

In this section, we investigate the stability of moving liquid sheets to externally varying pressure fields in an attempt to explain some of the experimental results reported in Sec. II. A time varying pressure field would accelerate the sheet perpendicular to its plane and could destabilize the sheet due to a RT type of instability. Our derivation of the model equations follows that of Keller and Kolodner[14] who derived the *inviscid flow* stability equations for a thin stationary liquid sheet accelerated perpendicular to its plane while ignoring the flow in the gas phase. Our analysis builds on the previous work by including the interaction of the liquid sheet with the surroundings by perturbing the flow in the gas phase while simultaneously accounting for motion of the liquid sheet both parallel and perpendicular to its plane. It is important to recognize at the outset that in our experiments, the sheet thickness varies spatially and the flow is radial. However, in order to capture the main effects of external acoustic forcing on such a flow, we simplify the situation to a constant thickness sheet moving in a rectilinear direction.

Consider then a thin liquid sheet of thickness h moving at a speed V in the horizontal (x) direction (Fig. 13). The acoustic source present on one side of the sheet sets a time varying pressure field far away from the sheet, $P_{\text{atm}}+P_m \cos(\omega t)$, while the pressure on the other side is atmospheric, P_{atm}. The difference in the pressure across the sheet imparts a vertical acceleration to the liquid sheet while

the liquid sheet moves in the transverse direction. If Φ and Θ are the velocity potentials in the liquid and gas phase, respectively, the pressure in each phase for inviscid flow is given by

$$\frac{p_l}{\rho_l} = \frac{\partial \Phi}{\partial t} - \frac{1}{2}(\nabla \Phi)^2,$$

$$\frac{p_a}{\rho_a} = \frac{\partial \Theta}{\partial t} - \frac{1}{2}(\nabla \Theta)^2. \tag{7}$$

The top ($i=1$) and bottom ($i=2$) interfaces of the film are prescribed by

$$z = F_i(x,y,t). \tag{8}$$

The normal stress balance at the liquid-gas interface ($z=F_i$) is given by

$$\rho_l\left\{\frac{\partial \Phi}{\partial t} - \frac{1}{2}(\nabla \Phi)^2 - (-1)^i \frac{\sigma_i 2H_i}{\rho_l}\right\} = \rho_a\left\{\frac{\partial \Theta}{\partial t} - \frac{1}{2}(\nabla \Theta)^2\right\}, \tag{9}$$

while the kinematic boundary condition at the interface $z=F_i$ in the two phases is obtained as

$$\frac{\partial \Phi}{\partial z} - \frac{\partial \Phi}{\partial x}\frac{\partial F_i}{\partial x} - \frac{\partial \Phi}{\partial y}\frac{\partial F_i}{\partial y} + \frac{\partial F_i}{\partial t} = 0, \tag{10}$$

$$\frac{\partial \Theta}{\partial z} - \frac{\partial \Theta}{\partial x}\frac{\partial F_i}{\partial x} - \frac{\partial \Theta}{\partial y}\frac{\partial F_i}{\partial y} + \frac{\partial F_i}{\partial t} = 0. \tag{11}$$

We assume a series expansion for the solution so that the zero order term corresponds to the base state, $\Phi=\Phi^0+\epsilon\Phi^1+\cdots$, $\Theta=\Theta^0+\epsilon\Theta^1+\cdots$, and $F_i=F_i^0+\epsilon F_i^1+\cdots$. For a liquid sheet moving simultaneously in the x direction with speed V and in the z direction with speed $u(t)$, the velocity potential (zeroth order) is given by

$$\Phi^0 = -u(t)z - Vx + b(t), \tag{12}$$

which on substitution in Eq. (7) gives

$$\frac{db}{dt} = \dot{u}F_i^0 + \frac{u^2}{2} + \frac{V^2}{2} + \frac{p_{a,i}}{\rho_l} \tag{13}$$

with the velocity in the z direction related to the sheet interface motion [from Eq. (10)], $u=dF_i^0/dt$. Note that since the sheet is undeformed the pressure in the liquid phase is the same as that in the gas phase. The liquid sheet thickness is given by $F_1^0-F_2^0=h$. The corresponding equations for the gas phase are

$$\Theta_i^0 = -u(t)z + c_i(t) \quad \text{and}$$

$$\frac{p_{a,i}}{\rho_a} = -\frac{1}{2}u(t)^2 - \dot{u}(t)F_i^o + \frac{dc_i}{dt}. \tag{14}$$

Since $p_{a,1}=0$ and $p_{a,2}=P_m\cos(\omega t)$, the external pressure can be related to the sheet acceleration using Eq. (14) and the normal stress balance condition, $\dot{u}(t)\rho_l h=P_m\cos(\omega t)$.

The first order solution is obtained by substituting the velocity potential and the sheet position in the series expansion in Eq. (9) and retaining terms linear in only first order,

$$\rho_l\left\{\frac{\partial \Phi}{\partial t} - \dot{u}F_i + u\Phi_z + V\Phi_x - (-1)^i\frac{\sigma_i \nabla^2 F_i}{\rho_l}\right\}_{z=F_i} = \rho_a\left\{\frac{\partial \Theta_i}{\partial t} + u(t)\frac{\partial \Theta_i}{\partial z} - \dot{u}(t)F_i\right\}_{z=F_i}. \tag{15}$$

The superscript "1" has been dropped for convenience. Similarly, the kinematic boundary conditions (10) and (11) reduce to

$$V\frac{\partial F_i}{\partial x} + \frac{\partial \Phi}{\partial z} + \frac{\partial F_i}{\partial t} = 0 \quad \text{on } z = F_i, \tag{16}$$

$$\frac{\partial \Theta_i}{\partial z} + \frac{\partial F_i}{\partial t} = 0 \quad \text{on } z = F_i. \tag{17}$$

Since Φ satisfies the Laplace equation, we assume the following form:

$$\Phi = \{g_1(t)e^{kz} + g_2(t)e^{-kz}\}\psi(x,y). \tag{18}$$

Consequently, Eq. (16) suggests the interface location, $F_i=f_i(t)\psi(x,y)$, so that from Eq. (17) we have

$$\frac{\partial \Theta_i}{\partial z} = -\frac{\partial f_i}{\partial t}\psi(x,y). \tag{19}$$

Further if we assume $\Theta_i(x,y,z,t)=(-1)^{i-1}\psi(x,y)s_i(z)\,\partial f_i/\partial t$, we have

$$\frac{ds_i}{dz}(z=F_i) = (-1)^i. \tag{20}$$

Also, Θ_i satisfies the Laplace equation,

$$\frac{\nabla^2\psi}{\psi} = -\frac{1}{s_i}\frac{\partial^2 s_i}{\partial z^2} = -k^2. \tag{21}$$

The above relation along with the boundary condition (20) suggest the following form for $s_i(z)$:

$$s_i(z) = \frac{e^{(-1)^i k(z-F_i)}}{k} \tag{22}$$

so that $s_1(z\to\infty)\to 0$ and $s_2(z\to-\infty)\to 0$.

On substituting the expression for Φ in Eq. (16), we have

$$\frac{k\{g_1 e^{kF_i^0} - g_2 e^{-kF_i^0}\} + \dot{f}_i}{Vf_i} = -\frac{\psi_x}{\psi}. \tag{23}$$

Since we will consider motion only in the x and z directions, we drop dependence on y so that $\psi(x)=\psi_o e^{ikx}$. On substituting $\psi(x)$, the above equation relates f_i and, g_1 and g_2,

$$g_1(t) = \frac{e^{-kF_1^0}}{k}\left\{\frac{(\dot{f}_2 e^{-kh} - \dot{f}_1) - ikV(f_1 - f_2 e^{-kh})}{1 - e^{-2kh}}\right\}, \tag{24}$$

$$g_2(t) = \frac{e^{kF_1^0}}{k}\left\{\frac{(\dot{f}_1 - \dot{f}_2 e^{kh}) - ikV(f_2 e^{kh} - f_1)}{1 - e^{2kh}}\right\}. \tag{25}$$

Similarly, Eq. (15) becomes

TABLE II. Measured sheet diameter and predicted film thickness at the edge of the sheet.

V (m/s)	We	D (m)	h (μm)
4.04	492	0.27	8.9
4.49	608	0.33	7.9
5.38	875	0.28	7.5
6.73	1368	0.24	10.2

$$\dot{g}_1 e^{kF_i^0} + \dot{g}_2 e^{-kF_i^0} - \dot{u} f_i + ku(g_1 e^{kF_i^0} - g_2 e^{-kF_i^0}) + ikV(g_1 e^{kF_i^0} + g_2 e^{-kF_i^0}) + (-1)^i \frac{k^2 T f_i}{\rho_l} + (-1)^i \frac{\rho_a}{\rho_l} \frac{1}{k} \frac{d^2 f_i}{dt^2} + \frac{\rho_a}{\rho_l}\left(u \frac{df_i}{dt} + \dot{u} f_i\right) = 0, \tag{26}$$

where the gravity term has been dropped. On substituting the above expressions for g_1 and g_2 along with that for Θ_i in the above equation gives two second order differential equations in terms of $f_+ = f_1 + f_2$ (sinuous mode) and $f_- = f_2 - f_1$ (dilatational mode),

$$\ddot{f}_+\left\{\tanh\left(\frac{kh}{2}\right) + \frac{\rho_a}{\rho_l}\right\} + \dot{f}_+\left\{2Vik \tanh\left(\frac{kh}{2}\right)\right\} + f_+\left\{-k^2V^2 \tanh\left(\frac{kh}{2}\right) + \frac{k^3\sigma}{\rho_l}\right\} = f_- \dot{u} k\left(1 - \frac{\rho_a}{\rho_l}\right) - \dot{f}_- \frac{\rho_a}{\rho_l} ku, \tag{27}$$

$$\ddot{f}_-\left\{\coth\left(\frac{kh}{2}\right) + \frac{\rho_a}{\rho_l}\right\} + \dot{f}_-\left\{2Vik \coth\left(\frac{kh}{2}\right)\right\} + f_-\left\{-k^2V^2 \coth\left(\frac{kh}{2}\right) + \frac{k^3\sigma}{\rho_l}\right\} = f_+ \dot{u} k\left(1 - \frac{\rho_a}{\rho_l}\right) - \dot{f}_+ \frac{\rho_a}{\rho_l} ku. \tag{28}$$

We recover the result of Squire (KH instability) on considering only the sinuous mode with $\dot{u} = u = 0$. The other limit of pure RT instability for an accelerating sheet[14] is obtained (in the absence of gravity) when the pressure difference across the sheet is assumed to be a constant and both the density of air and the transverse velocity of the sheet are set to zero.

For small forcing, an approximate solution to Eqs. (27) and (28) is possible using method of multiple scales. The asymptotic solution, which is given in the Appendix, demonstrates two distinct time scales corresponding to the sinuous and the dilatational modes. The predicted threshold value of SPL at which instability occurs decreases with We and increases with ω, both in qualitative agreement with the experimental observations. However, the threshold value is an order of magnitude lower while the predicted wavelengths are higher than those observed. These discrepancies are not surprising since the experimental conditions correspond to finite forcing which motivates the need for full numerical solution of the governing equations for comparison with experimental results.

IV. COMPUTATIONAL RESULTS

The governing Eqs. (27) and (28) are solved using the Floquet theory which states that for a system of equations of the form

$$\mathbf{A}(t) f(t) = \mathbf{B} f'(t), \tag{29}$$

where $f(t)$ is the unknown function of time, $\mathbf{A}(t)$ is a continuous T periodic matrix, and $\mathbf{B}$ is a constant matrix, there exists a constant matrix $\mathbf{R}$ such that

$$\mathbf{S}(t+T) = \mathbf{R}\mathbf{S}(t). \tag{30}$$

Here, $\mathbf{S}(t)$ is the fundamental solution matrix satisfying Eq. (29). Further, if the characteristic roots of $\mathbf{R}$ are $\lambda_i, i = 1, 2, \ldots$, then the solution of Eq. (29) can be written as

$$x_i = e^{\gamma_i t} z_i(t) \quad \text{with} \quad z_i(t+T) = z_i(t),$$

where the characteristic exponents γ_i are related to the characteristic roots by

$$\gamma_i = \frac{1}{T} \ln(\lambda_i).$$

Since $\mathbf{S}(T) = \mathbf{R}\mathbf{S}(0)$, $\mathbf{R}$ can be obtained by integrating Eq. (30) over one period with $\mathbf{S}(0) = \mathbf{I}$, where $\mathbf{I}$ is the identity matrix. The stability property is determined by the sign of γ_i. The flow is linearly unstable if the real part of γ_i is positive; if it is negative the flow is stable. Otherwise the flow is neutrally stable. The imaginary part of γ_i determines the frequency response of the perturbed flow to the periodic forcing. Further, it is assumed that the physically observable growth rate will correspond to the wavenumber with the largest positive value of the real part of γ_i.

The simulations were performed for the We = 608 (stable regime) and 1350 (flapping regime), sheet thicknesses of 7 and 100 μm and varying frequencies and dimensionless wavenumber ($x = kh/2$). While the latter thickness applies to regions close to the point of impingement, the former is representative of the outer edge of the sheet (see Table II). All the computations were performed at SPL of 100 dB, which corresponds to peak pressure of 2.83 Pa ($P_m d_o/\sigma = 0.085$).

The predicted maximum growth rates are plotted in Fig. 14 against the respective frequencies and wavelengths for 7 μm thickness sheets. For comparison, we have also plotted the sinuous and dilatational growth rates in the absence of forcing (purely KH instability). At We = 608, the dilatational growth rate is much larger than the sinuous mode for the KH instability [Fig. 14(a)]. For the pure KH case, it is well known that the sinuous mode is always stable for $\mathrm{We}_s < 2$, whereas the dilatational mode will be unstable. For We = 608 in Fig. 14(a), $\mathrm{We}_s = 1.97$ implying that the sinuous mode is stable. However, even the maximum dilatational growth rate in the absence of acoustics (pure KH case) is two orders of magnitude lower than the peak values in the presence of acoustics [Fig. 14(b)]. Further, two distinct peaks in growth rates at a fixed forcing frequency are observed.

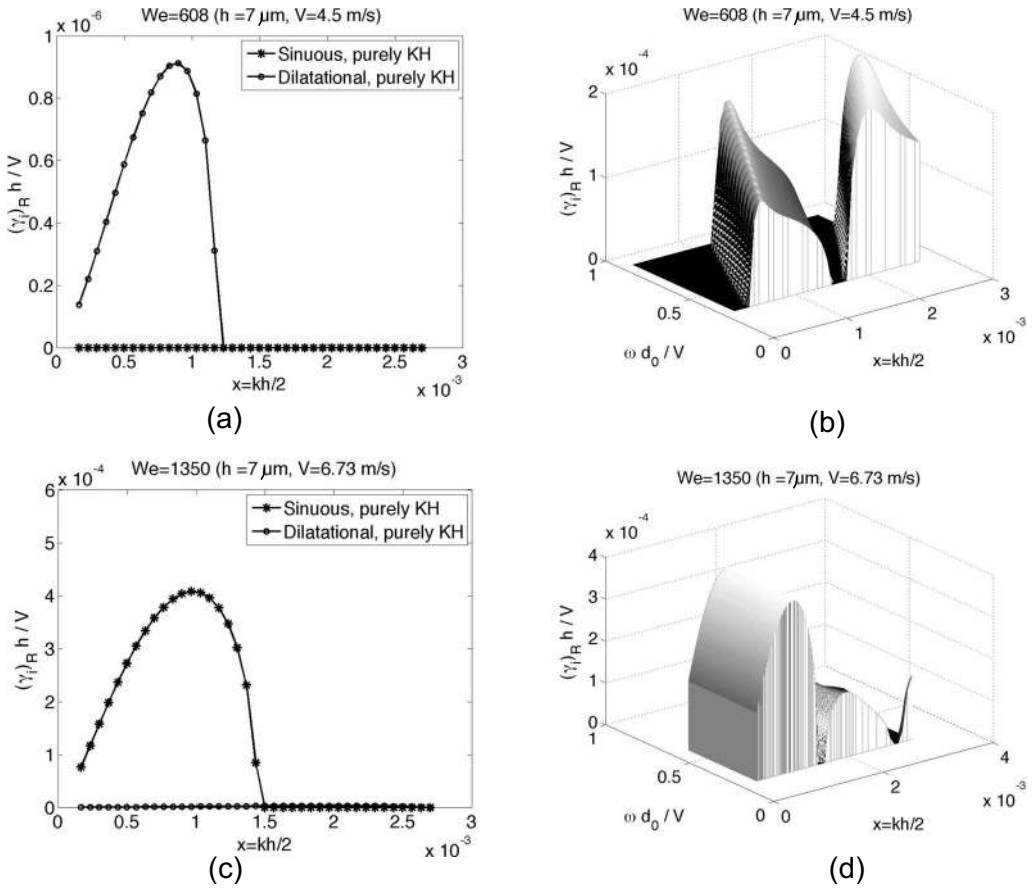

FIG. 14. The dimensionless maximum growth rate plotted as a function of $x=kh/2$ and $\omega d_o/V$ for a sheet of thickness 7 μm, and $V=4.5$ m/s (We=608), (a) without and (b) with forcing. Similarly, for $V=6.73$ m/s (We=1350), (c) without and (d) with forcing.

The magnitude of the second peak at the larger value of x is higher suggesting that the forcing will result in wavelengths that are smaller than that predicted in the absence of acoustics (KH instability). If the droplets are assumed to be related to this wavelength then the prediction is in line with the experimental observation where the drop size reduced significantly under forcing. Note further that the magnitude of the sinuous and dilatational modes are comparable unlike in the case of KH instability. The variation of the growth rates of the two modes with frequency will be discussed later.

At higher liquid velocity but at the same SPL, the magnitude of the growth rates due to KH instability becomes significant. This is evident on comparing We=1350 for the KH case [Fig. 14(c)] with that under forcing [Fig. 14(d)] where the growth rates for the two cases match for $x<1.5\times10^{-3}$. The lower peaks at higher x are from the periodic forcing. Thus for a constant thickness, the growth rates for the periodic forcing are much higher at lower velocities, which explains the strong influence of acoustics for all Weber numbers except We=1350 (the peak in growth rate here is set by the KH instability). Not only does the growth rate of the KH instability increases with We but the wavelength for the maximum growth rate for the KH instability also decreases.

At a fixed velocity, the thicker sheet is less affected by the forcing compared to the KH instability since the acceleration imparted by the forcing goes as, $P_m/\rho_l h$. This is evident from the comparison of growth rates for 100 μm (Fig. 15) where the dimensional growth rates for the periodic forcing is almost an order of magnitude lower than that due to KH instability. Again, the peaks due to the KH instability match in the two-dimensional (2D) and 3D plots.

V. COMPARISON WITH EXPERIMENTS

Recall that the observed wavelengths of the ripples in the radial direction are $\lambda\sim0.011-0.014$ m. Figure 16(a) plots the most unstable wavelength as a function of the dimensionless frequency for $h=7$ μm, which corresponds to the edge of the sheet (results for $h=10$ μm are similar). The predicted values lie close to the observed range (indicated by two horizontal dotted lines). On the other hand, the purely KH instability wavelengths (i.e., in the absence of forcing) are twice the measured values and the growth rates are two orders of magnitude lower than those in the presence of acoustics [Fig. 16(b)]. The zero frequency case, also plotted in Fig. 16(b) and which Bremond *et al.*[12] consider (purely RT instability), results in a flat growth rate curve in the ROI and does not yield a unique wavelength. While Bremond *et al.*[12] attributed the wavelength selection to extraneous factors, such as the roughness of the injecting device, the most unstable wavelength in our case is determined uniquely by the parametric resonance. This applies also to a periodically

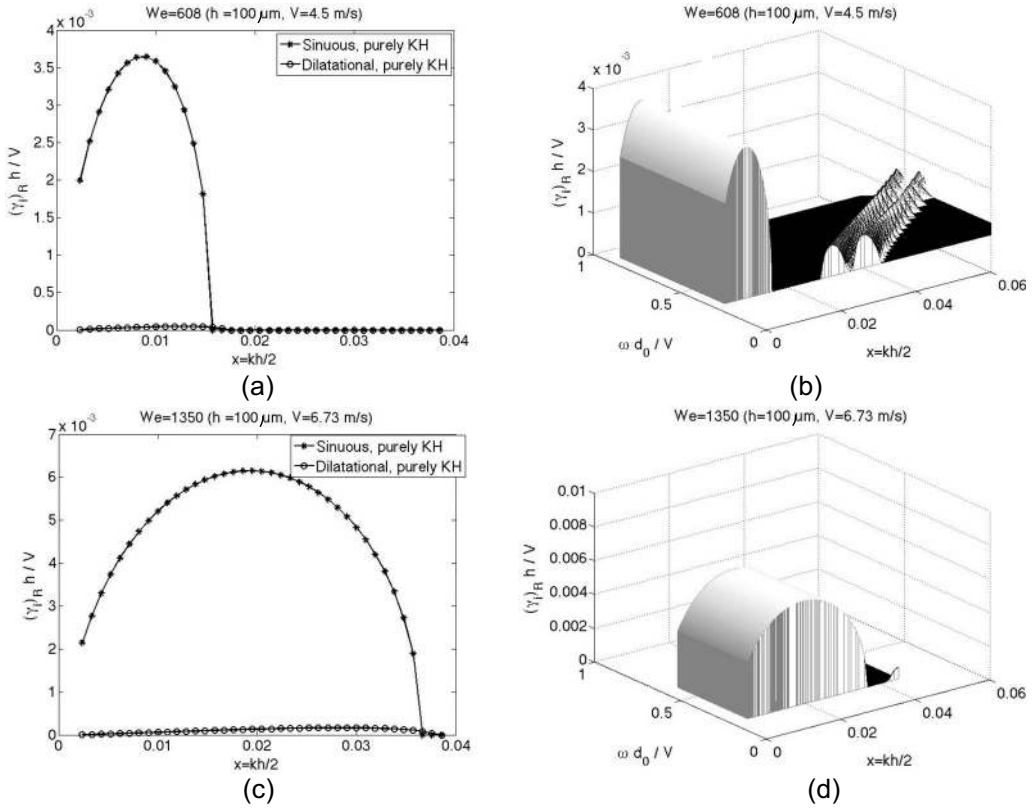

FIG. 15. The dimensionless maximum growth rate plotted as a function of $x=kh/2$ and $\omega d_o/V$ for a sheet of thickness 100 μm, and $V=4.5$ m/s (We=608), (a) without and (b) with forcing. Similarly, for $V=6.73$ m/s (We=1350), (c) without and (d) with forcing.

forced stationary liquid sheet [$V=0$, $\omega=691.1$ rad/s in Fig. 16(b)], which shows a peak growth rate at a unique wavelength.

The question now arises if the pronounced response observed at selected frequencies can be predicted by the model calculations. Note that this trend is also observed for other Weber numbers (Fig. 7) where the SPL to induce response is nonmonotonic in the frequency range of $\omega d_o/V=0.3-1.0$. Recall that We<800 corresponds to the stable sheet regime where the balance of surface tension and inertial forces at the rim sets the sheet diameter. The sheet surface is smooth and is not significantly perturbed by the KH instability. In our experiments, the thickness close to the edge of the sheet is of the order of 10 μm and a rim of a few millimeter thickness borders the sheet. Consequently, the displacement of the rim is expected to be at least two orders of magnitude lower than the rest of the sheet. Therefore, the rim is displaced negligibly by the external forcing compared to the rest of the sheet. The situation is identical to a circular elastic sheet that is pinned at the edges which is capable of supporting standing waves. This is somewhat similar to the case studied by Benjamin and Ursell[15] who showed that the liquid surface is excited at only those frequencies that corresponded to the spatial modes supported by the geometry of the container. The differential equation for the spatial mode of the ripples can be obtained in one dimension on solving Eq. (21) with the boundary conditions of symmetry at the center and negligible displacement at the edges. The solution gives the spatial modes of the system as $\cos(k_m D/2)=0$, where $k_m=(2m+1)\pi/D$ and $m=1,2,\ldots$. For simplicity, we use the cosine function instead of the Bessel function as the zeros of the two functions are nearly equal for large m. Figure 17 presents separately for We=608 and $h=7$ μm, the 2D plots of the most unstable mode for selected spatial modes ($m=22-25$) that exhibit significant growth rates. For a given spatial mode, the growth rate consists of large regions of high growth rate interspersed by regions of negligible rates. The trend seems to suggest that the sheet will break up over a certain range of forcing frequencies if the frequency lies in regions of high growth rates. The plot also includes vertical arrows that indicate the frequencies at which the sheet responded significantly in our experiments to the acoustics. Although the observed frequencies lie in the range predicted by the model, no response was recorded at higher frequencies ($0.5<\omega d_o/V<0.9$), where the predicted growth rates are higher. Thus the agreement between the observations and predictions is only qualitative and more work is required to ascertain the reasons behind these discrepancies. However, the model predictions are in line with those of the nonlinear stability analysis by Jazayeri and Li[16] of a moving plane liquid sheet (in the absence of acoustics) who used a perturbation expansion technique and showed that while the most unstable mode at the lowest order is sinuous (linear stability), the thinning and subsequent breakup of the sheet is caused by the second order term that is dilatational in nature. This suggests that in our case, the external varying pressure

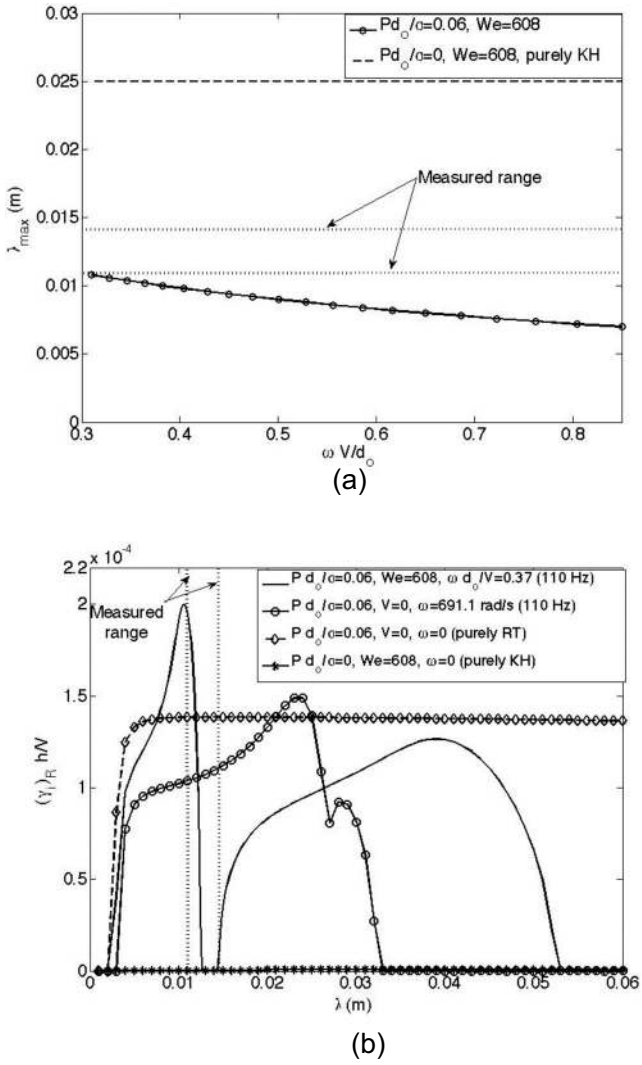

FIG. 16. (a) Comparison of the most unstable wavelength for $h=7$ μm with measurements. The wavelength predicted from the purely KH instability is included for comparison. (b) Growth rate for a moving sheet under periodic forcing, a stationary sheet under forcing, a purely RT, and a purely KH instability.

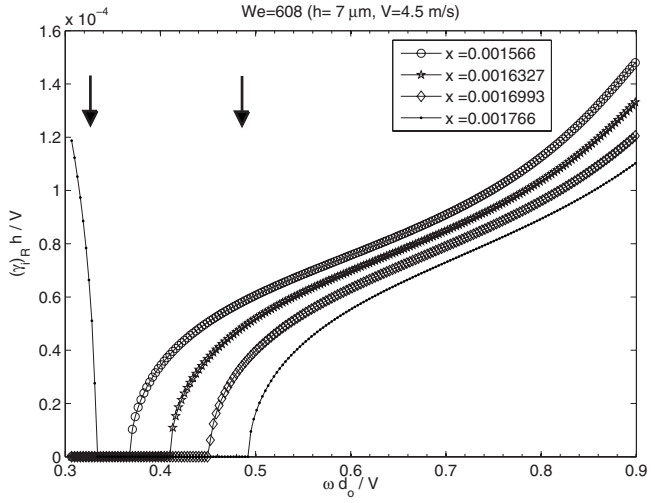

FIG. 17. Dimensionless growth rate plotted as a function of dimensionless forcing frequency for a sheet of thickness 7 μm and $V=4.5$ m/s (We=608) for $x=0.001\,566$ ($m=22$), $0.001\,633$ ($m=23$), $0.001\,699$ ($m=24$), and $0.001\,766$ ($m=25$). These values of x fall within the measured range. The arrows indicate the frequencies at which significant sheet reduction was observed.

field couples the sinuous and dilatational modes at the lowest order leading to an early breakup.

A close look at the second quadrant of the circular sheet in Fig. 5 reveals radial streaks separated at a distance of 0.008–0.012 m just before breakup. It is possible that the streaks are a result of the sheet becoming unstable in the azimuthal direction also. Further, once the sheet reaches a stable diameter under acoustic forcing, the droplets either detach from the rim as observed in the stable regime or are ejected in form of a fine spray at discrete locations along the rim of the sheet. These observations indicate that the measured drop size distribution is an outcome of a complex process of atomization, which may not be captured by the linear stability analysis presented here. The ripples observed in our experiment, in all probability, are caused by the superposition of various unstable modes. While it is not possible to ascertain the exact spatial modes excited by the acoustics, the qualitative agreement between the observed wavelength of the surface ripples (0.011–0.014 m) and that of the spatial modes in Fig. 17 lends support to the proposed mechanism.

Simulations were also performed to determine the critical pressure for a constant growth rate and for varying frequency at the experimentally observed wavenumbers. While the pressure showed peaks at selected frequencies, as expected from the trend in Fig. 17, we are unable to predict numerically the observed increase in the critical SPL variation with forcing frequency. In fact our simulations show that for a fixed thickness, wavelength, and liquid velocity, the growth rate increases with frequency. Kumar[17] predicts increasing forcing amplitude with frequency for *stationary* liquid sheets and attributes it to the viscous dissipation. However, their numerical simulations for thick sheets ($\sim$1 mm) for high frequencies ($\sim$10 kHz) show an almost linear increase with applied frequency. These results along with the fact that the liquid sheet thickness varies spatially and is moving underscores the need for solving the viscous momentum equation along with determining the stability of the film to spatially growing instabilities in the film.

VI. CONCLUSION

We study the influence of acoustics on thin planar liquid sheets formed by impinging two collinear water jets. Experiments have been performed over a range of We, forcing frequency and SPL. For a given We and acoustic frequency, there is a threshold SPL below which the sheet will not respond. The threshold SPL appears to scale as the square of the forcing frequency. For experiments conducted at a fixed sound intensity of 100 dB ($Pd_o/\sigma=0.06$), the sheet responded to external forcing for We=492, 608, 875, and 1350. Further, the sheet showed pronounced response at selected frequencies. The droplet size reduced significantly and the shedding frequency was close to the forcing frequency in some cases.

The model of Squire[1] was extended to account for the influence of the external pressure forcing on a liquid sheet of constant thickness. The model equations show that the sinuous and the dilatational modes are coupled, which is in contrast with the KH instability, where the growth rates for the dilatational modes are negligibly small. The Floquet analysis was employed to determine the maximum growth rate for a given set of parameters. At a constant thickness, the growth rates for the periodic forcing are higher at lower velocities, which explains the importance of periodic forcing over the KH instability. On the other hand, at a fixed velocity, the thicker sheet is less affected by the forcing compared to the KH instability. The simulations predict maximum growth rates at wavenumbers close to those observed in the experiments. However, the model was neither able to predict the observed variation of SPL with forcing frequency nor was it able to reproduce the pronounced response at discrete frequencies. Clearly, more work is needed to clarify these issues.

ACKNOWLEDGMENTS

The authors acknowledge the financial assistance from the Indian Institute of Technology-Bombay under Grant No. 05IS002. The authors thank Saurav Jha for the help with the drop size and shedding frequency analysis and Dr. N. Ananthakrishnan and Professor S. D. Sharma for useful discussions during their initial involvement with the investigation.

APPENDIX: MULTIPLE SCALE ANALYSIS FOR THE COUPLING OF SINUOUS AND DILATATIONAL MODES

Equations (27) and (28) are reminiscent of the Mathieus equation for an oscillating pendulum with a periodically varying length except that in our case, the periodicity comes from the coupling of the sinuous and dilatational modes. Consequently, we attempt an approximate solution using the method of multiple scales in manner similar to those for the Mathieus equation. The response of the sheet at selected frequencies, the existence of a threshold value of SPL only above which the sheet responds to external forcing, and the variation of threshold SPL with We is simulated by an asymptotic analysis of the equations governing the evolution of waveforms of the sheet. The main step of the solution procedure is to recognize the existence of two distinct time scales at which the amplitude of the sinuous and dilatational mode varies. There is a fast time scale at which the amplitude oscillates while a much longer time scale at the which the amplitude drifts. While the former occurs at inverse of the eigenvalues of Eqs. (27) and (28) obtained in the absence of the external pressure variation, the latter is the result of the coupling between the two modes.

We proceed by rendering Eqs. (27) and (28) dimensionless,

$$\ddot{f}_+(z+r)+\dot{f}_+2\alpha z i+f_+(\beta-\alpha^2 z)=(1-r)\zeta f_-\cos\bar{t}-r\zeta\dot{f}_-\sin\bar{t}, \tag{A1}$$

$$\ddot{f}_-(1+zr)+\dot{f}_-2\alpha i+f_-(\beta z-\alpha^2)=(1-r)z\zeta f_+\cos\bar{t}-zr\zeta\dot{f}_+\sin\bar{t}, \tag{A2}$$

where $\zeta=P_m k/\rho_l\omega^2 h$, $z=\tanh(kh/2)$, $\alpha=kV/\omega$, $\bar{t}=\omega t$, $r=\rho_a/\rho_l$, and $\beta=k^3\sigma/\rho_l\omega^2$. We look for a solution of the forms $f_+(\bar{t};\zeta)=f_+(T_0,T_1;\zeta)$ and $f_-(\bar{t};\zeta)=f_-(T_0,T_1;\zeta)$, where $T_0=\bar{t}$ is the fast time scale and $T_1=\zeta\bar{t}$ is the slow time scale. We propose an expansion in f_+ and f_- for $\zeta\ll 1$,

$$f_+(\bar{t};\zeta)=f_+^0(T_0,T_1)+\zeta f_+^1(T_0,T_1)+\cdots, \tag{A3}$$

$$f_-(\bar{t};\zeta)=f_-^0(T_0,T_1)+\zeta f_-^1(T_0,T_1)+\cdots. \tag{A4}$$

Substituting the above expansion in Eqs. (A1) and (A2) and comparing coefficients of ζ^n, we obtain a sequence of problems.

At ζ^0,

$$\mathcal{D}_0^2 f_+^0(z+r)+\mathcal{D}_0^1 f_+^0 2\alpha z i+f_+^0(\beta-\alpha^2 z)=0, \tag{A5}$$

$$\mathcal{D}_0^2 f_-^0(1+zr)+\mathcal{D}_0^1 f_-^0 2\alpha i+f_-^0(\beta z-\alpha^2)=0. \tag{A6}$$

Here, $\mathcal{D}_0^1\equiv\partial/\partial T_0$, $\mathcal{D}_0^2\equiv\partial^2/\partial T_0^2$, etc. Integrating with respect to T_0 and treating T_1 as an independent variable held constant, we obtain a general solution,

$$f_+^0=A_1(T_1)e^{ia_1T_0}+A_2(T_1)e^{ia_2T_0}, \tag{A7}$$

$$f_-^0=B_1(T_1)e^{ib_1T_0}+B_2(T_1)e^{ib_2T_0}, \tag{A8}$$

where $a_{i=1,2}$ and $b_{i=1,2}$ are the eigenvalues for sinuous and dilatational modes for the KH instability in the absence of the external pressure, respectively.

At ζ^1,

$$\mathcal{D}_0^2 f_+^1(z+r)+\mathcal{D}_0^1 f_+^1 2\alpha z i+f_+^1(\beta-\alpha^2 z)=-2(z+r)\mathcal{D}_0\mathcal{D}_1 f_+^0-2\alpha z i D_1 f_+^0+\frac{f_-^0}{2}(e^{it}+e^{-it}), \tag{A9}$$

$$\mathcal{D}_0^2 f_-^1(1+zr)+\mathcal{D}_0^1 f_-^1 2\alpha i+f_-^1(\beta z-\alpha^2)=-2(1+zr)\mathcal{D}_0\mathcal{D}_1 f_-^0-2\alpha i D_1 f_-^0+z\frac{f_+^0}{2}(e^{it}+e^{-it}). \tag{A10}$$

Since for our case $r\ll 1$ we have dropped the $\sin\bar{t}$ term on the right hand side of Eqs. (A1) and (A2). Substituting Eqs. (A7) and (A8) in the above two equations we recognize that resonance arising from the coupling is possible when

$$a_i=b_i+1. \tag{A11}$$

In the case of $a_i\approx b_i+1$, we introduce a detuning parameter[18] Σ defined by $a_i=b_i+1+\zeta\Sigma$ to determine the bounds for stable forcing. Substituting this new expression for a_i in Eqs. (A9) and (A10) and applying the secularity condition that the asymptoticness is not lost when $T_1=\mathcal{O}(1)$ gives a differential equation for A_1,

$$\mathcal{D}_1^2 A_1 + i\Sigma D_1^1 A_1 + \gamma A_1 = 0, \quad \text{where} \tag{A12}$$

$$\gamma = \frac{z}{16[(1+zr)b_i + \alpha][(z+r)a_i + \alpha z]}.$$

Substituting $A_1 = e^{i\Gamma T_1}$ in the above equation gives $\Gamma = (-\Sigma \pm \sqrt{\Sigma^2 + 4\gamma})/2$. Thus the coupling leads to instability when $\Sigma^2 + 4\gamma < 0$. Consequently, substitution of a_i and b_i in the expression for γ gives two possible combinations of eigenvalues at which instability could occur, namely, $a_1 = b_2 + 1 + \Sigma\zeta$ or $a_2 = b_1 + 1 + \Sigma\zeta$ with

$$\gamma = -\frac{1}{16}\frac{z}{\sqrt{[\alpha^2 + (1+zr)(\beta z - \alpha^2)][\alpha^2 z^2 + (z+r)(\beta - \alpha^2 z)]}}.$$

The line of neutral stability and therefore the transition curve is obtained from $\Sigma^2 + 4\gamma = 0$,

$$a_1 = b_2 + 1 \pm 2\sqrt{|\gamma|}\zeta, \tag{A13}$$

$$a_2 = b_1 + 1 \pm 2\sqrt{|\gamma|}\zeta. \tag{A14}$$

The asymptotic solution [Eqs. (A13) and (A14)] represents transition curves that divide the pressure-frequency plane into regions of stability and instability. The approximate analysis also gives the growth rate of the instability for low forcing (ζ) and negligible liquid velocities. The growth rate on coupling of the sinuous and dilatational modes attains the highest value for $\Sigma = 0$, $\Gamma = \sqrt{|\gamma|}$. On neglecting interactions with surrounding air ($r = 0$), the dimensional growth rate becomes $\sqrt{P_m^2/16k\sigma h^2\rho_l}$ (root mean square pressure is related to the peak pressure, $P_m = P\sqrt{2}$). If we assume that sheet will become unstable when the flow time scale is of the order of the inverse of growth rate, the critical SPL (P_c) becomes

$$\sqrt{\frac{P_c^2}{8k\sigma h^2\rho_l}} \sim \frac{2V}{D}. \tag{A15}$$

The wavenumber is related to the applied forcing frequency by the resonance condition, Eq. (A11), $k = \omega\sqrt{\rho_l h/2\sigma}$. For low We, the diameter of the sheet is related by Eq. (1), giving

$$\frac{P_c d_o}{\sigma} \sim 8\sqrt{2}\frac{(\omega d_o/V)^{1/2}}{We^{7/4}}. \tag{A16}$$

The above scaling predicts that the critical SPL decreases with We and increases with ω, both in qualitative agreement with the observation (Fig. 7). However the prediction is about an order of magnitude lower and the increase with frequency is much slower ($\sqrt{\omega}$) than that observed ($\sim\omega^2$). Further, the predicted wavelength $\lambda = 2\pi/k \sim 0.04$ m is higher than measured values (0.011–0.014 m). These discrepancies are not surprising since the experimental conditions correspond to $\zeta \sim \mathcal{O}(1)$, which motivates the need for full numerical solution of the governing equations for comparison with experimental results.

We would like to note that the "wavy corridor" mechanism suggested by Bremond *et al.*[12] for the breakup of liquids sheets oscillated using a jet impactor is different from the coupling mechanism suggested here. Their analysis based on transient accelerations imparted to the sheet involving a centrifugal instability of a RT type suggests a growth rate that varies as $\sqrt{\rho h\gamma^2/2\sigma}$, where γ is the imposed sheet acceleration. On the other hand, the parametric resonance predicted by our analysis results in a growth rate (asymptotic solution) which is different, $\sqrt{\rho\gamma^2/16\sigma k}$, where k is related to the thickness via the resonance condition, $k = \omega\sqrt{\rho_l h/2\sigma}$. Further, they showed that for a fixed jet velocity and imposed amplitude of oscillation, the radius of the sheet reduces monotonically with increasing imposed frequency. The present results show that on solving the full equations, the sheet reduction occurs over a selected range of frequencies when it is exposed to external acoustics.

[1] H. B. Squire, "Investigation of the instability of a moving liquid film," Br. J. Appl. Phys. **4**, 167 (1953).
[2] G. I. Taylor, "The dynamics of thin sheets of fluid. II. Waves on fluid sheets," Proc. R. Soc. London, Ser. A **253**, 296 (1959).
[3] G. I. Taylor, "The dynamics of thin sheets of fluid. III. Disintegration of fluid sheets," Proc. R. Soc. London, Ser. A **253**, 313 (1959).
[4] J. C. P. Huang, "The break-up of axisymmetric liquid sheets," J. Fluid Mech. **43**, 305 (1970).
[5] D. Weihs, "Stability of thin, radially moving liquid sheets," J. Fluid Mech. **87**, 289 (1978).
[6] A small disturbance in the center of the circular expanding sheet forms two cardioidal wave lines.
[7] E. Villermaux and C. Clanet, "Life of flapping liquid sheet," J. Fluid Mech. **462**, 341 (2002).
[8] C. Clanet and E. Villermaux, "Life of smooth liquid sheet," J. Fluid Mech. **462**, 307 (2002).
[9] W. A. Sirignano and C. Mehring, "Review of theory of distortion and disintegration of liquid streams," Prog. Energy Combust Sci. **26**, 609 (2000).
[10] N. O. Rhys, "Acoustic excitation and destruction of liquid sheets," Ph.D. thesis, University of Alabama, 1999.
[11] V. Sivadas, E. C. Fernandes, and M. V. Heitor, "Acoustically excited air-assisted liquid sheets," Exp. Fluids **34**, 736 (2003).
[12] N. Bremond, C. Clanet, and E. Villermaux, "Atomization of undulating liquid sheets," J. Fluid Mech. **585**, 421 (2007).
[13] E. Villermaux, Ph. Marmottant, and J. Duplat, "Ligament-mediated spray formation," Phys. Rev. Lett. **92**, 074501 (2004).
[14] J. B. Keller and I. Kolodner, "Instability of liquid surfaces and the formation of drops," J. Appl. Phys. **25**, 918 (1954).
[15] T. B. Benjamin and F. Ursell, "The stability of the plane free surface of a liquid in vertical periodic motion," Proc. R. Soc. London, Ser. A **225**, 505 (1954).
[16] S. A. Jazayeri and X Li, "Nonlinear instability of plane liquid sheets," J. Fluid Mech. **406**, 281 (2000).
[17] K. Kumar, "Parametric instability of a liquid sheet," Proc. R. Soc. London, Ser. A **457**, 1315 (2001).
[18] A. H. Nayfeh and D. T. Mook, *Nonlinear Oscillations* (Wiley, New York, 1979).